AIP | Applied Physics Letters

Fracture dynamics in implanted silicon

D. Massy, F. Mazen, S. Tardif, J. D. Penot, J. Ragani, F. Madeira, D. Landru, O. Kononchuk, and F. Rieutord

Citation: Applied Physics Letters **107**, 092102 (2015); doi: 10.1063/1.4930016
View online: http://dx.doi.org/10.1063/1.4930016
View Table of Contents: http://scitation.aip.org/content/aip/journal/apl/107/9?ver=pdfcov
Published by the AIP Publishing

Fracture dynamics in implanted silicon

D. Massy,[1,2] F. Mazen,[1,3] S. Tardif,[1,2] J. D. Penot,[1,2] J. Ragani,[1,2] F. Madeira,[1,3] D. Landru,[4] O. Kononchuk,[4] and F. Rieutord[1,2]
[1]*Univ. Grenoble Alpes, F-38000 Grenoble, France*
[2]*CEA, INAC-SP2M, F-38000 Grenoble, France*
[3]*CEA, LETI, MINATEC Campus, F-38054 Grenoble, France*
[4]*SOITEC, Parc Technologique des Fontaines, 38190 Bernin, France*

(Received 13 May 2015; accepted 17 August 2015; published online 2 September 2015)

Crack propagation in implanted silicon for thin layer transfer is experimentally studied. The crack propagation velocity as a function of split temperature is measured using a designed optical setup. Interferometric measurement of the gap opening is performed dynamically and shows an oscillatory crack "wake" with a typical wavelength in the centimetre range. The dynamics of this motion is modelled using beam elasticity and thermodynamics. The modelling demonstrates the key role of external atmospheric pressure during crack propagation. A quantification of the amount of gas trapped inside pre-existing microcracks and released during the fracture is made possible, with results consistent with previous studies. © *2015 AIP Publishing LLC*.
[http://dx.doi.org/10.1063/1.4930016]

The Smart Cut™ technology[1] is currently the industry standard for manufacturing Silicon-On-Insulator (SOI) substrates, widely used in most recent microelectronics devices. The implantation of relatively high doses of gas ions in a thermally oxidized silicon substrate leads to the formation of a buried weakened layer in the crystal. The implanted wafer is then bonded onto a host substrate using direct wafer bonding. Under annealing, the implanted species evolve into microcracks lying parallel to the surface,[2] and a controlled fracture process finally occurs along the implanted layer.

The detailed microscopic evolution of platelets and microcracks has been extensively studied by a number of techniques including X-rays and electron microscopy.[3–6] The analysis of microcracks development provides criteria for fracture initiation[7] but gives no clue on what happens during macroscopic crack propagation. While Si/SiO_2 direct wafer bonding statics and dynamics are now well understood,[8–10] the fracture dynamics during Smart Cut™ remains largely a field to be explored. Yet, the ever decreasing thickness of SOI substrates requested by the microelectronics industry calls for a multiscale understanding and control of the fracture step. Wafer-scale fracture being the last key step of SOI manufacturing, it impacts directly the SOI active layer properties by revealing the underlying crack microstructures and interactions.[11]

Fracture waves in brittle solids have a high velocity, typically on the order of a few kilometres per second, which renders the study of their propagation quite difficult. So far, monitoring of dynamic fracture in brittle materials has mainly been performed using high speed photography in transparent samples[12,13] or fracture gauges, i.e., measuring the resistance change of a thin conductive coating layer deposited at least on one side of the sample.[14–17] To perform these experiments, a notch is usually introduced on the specimen and the fracture is initiated by loading a wedge or using a traction tool. Information on the crack front shape can also be deduced afterwards by analysing the "Wallner lines" or the crack front waves.[18–20] In this paper, we first present an original device for direct measurements of fracture velocity and crack opening displacement in silicon samples without any use of conductive layer coating. Then, an example of interferometric measurement of the specimen deformation behind the fracture front is shown and used to illustrate the fracture dynamics modelling in the Smart Cut™ technology. Fracture dynamics in implanted materials involves similar stress fields than standard brittle fracture in test machines. The only difference is that the crystal is subjected to internal stress due to implantation defects (pressurized microcracks) acting on crack faces rather than, e.g., externally applied stress. It is energetically much easier for the fracture to progress along the weakened layer where the area covered by the microcracks can reach up to 60% of the sample surface.[2] The modelling presented in the second part of the paper shows the key role of the trapped hydrogen gas that tends to separate the two bonded wafers. Such phenomenon does not exist in crystalline silicon cleavage, but the original approach presented here may be used to monitor fracture dynamics in more general cases.

Our optical measurement of the fracture wave velocity is based on the transmission monitoring of infrared lasers through the silicon sample. An infrared laser diode ($\lambda = 1310$ nm) connected to an optical fiber multiplexer outputs four laser beams which are then sent through the sample using fiber-coupled lenses. Since silicon is transparent at this wavelength, the infrared beams are collected on the other side of the sample using fiber-coupled lenses on the receiver part. Fast InGaAs photodiodes are used to convert the transmitted light into electrical signals which are recorded using a high bandwidth numerical oscilloscope as shown in Fig. 1. The sample holder includes a blade which can be inserted at the bevelled edge of the silicon bar, allowing mechanical fracture initiation by pushing slowly the blade into the sample. The setup can also be used with an adapted oven (not shown on the scheme) that lets the laser beams through. In this case, the sample holder is put inside the oven and

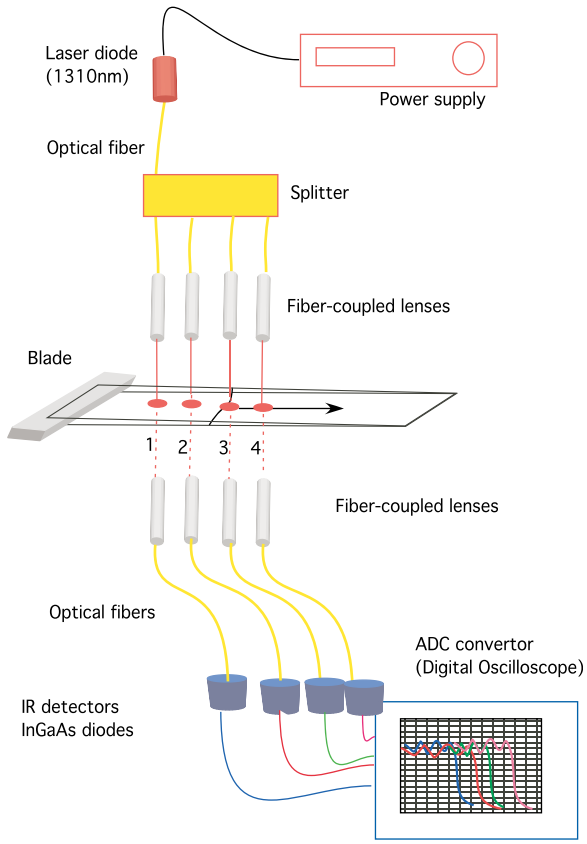

FIG. 1. Experimental setup for crack front velocity measurements.

fracture initiation can occur either thermally or mechanically. This configuration allows the independent control of fracture initiation at any desired temperature. Here, this patented optical bench[21] is used to determinate the fracture velocity in the Smart Cut™ technology.

A typical signal recorded during the experiment is shown in Fig. 2. The illustrative silicon sample consists of a $20 \times 90\,\text{mm}^2$ silicon strip cuts out along the [110] direction of a 300 mm bonded silicon (100) wafer.[22–26] The single wafer thickness h is equal to 775 μm so the total thickness of the strip is 1.55 mm. The dose of implanted hydrogen before bonding was 5.75×10^{16} H^+/cm^2 at an energy of 32 keV. This sample was first annealed at 425 °C for 100 min to develop microcracks in the implanted layer and then mounted on the sample holder inside the oven. Smart Cut™ was mechanically initiated at some time at 110 °C.

Initially, the intensity received on the detector is constant since the two wafers are still bonded. The opening gap creates two new surfaces where the laser beam can be partially reflected. Therefore, when the crack front reaches the laser location, the signal intensity drops as shown in Fig. 2. This sudden variation of intensity is used to trigger the recording of the oscilloscope. The following part of the transmitted signal is made of series of intensity oscillations with varying periods.

By measuring the time lags between the intensity drops on each laser signal, three fracture velocities between the four laser locations on the sample can be deduced. In our example, the annealing thermal budget and split temperatures were large enough to generate a self-propagating

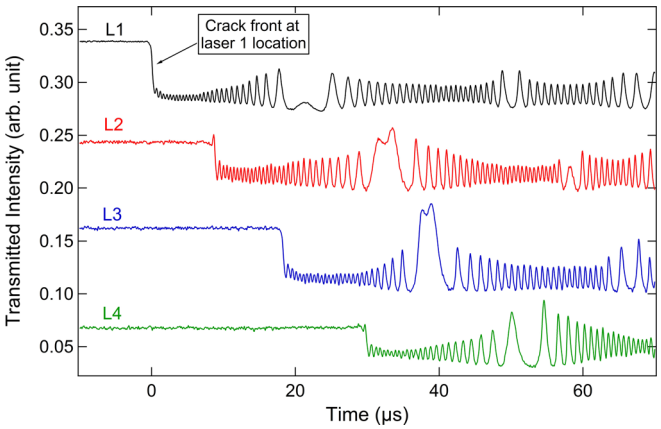

FIG. 2. Laser interferences due to crack opening gap recorded during the crack propagation.

fracture wave that quickly reaches an asymptotic speed, hence giving same values for the different positions:

$$v_{12} = 1.8 \pm 0.1\,\text{km s}^{-1}, \quad v_{23} = 1.7 \pm 0.1\,\text{km s}^{-1},$$
$$v_{34} = 1.7 \pm 0.1\,\text{km s}^{-1}.$$

The classical expression for the asymptotic crack velocity reads[27]

$$v = v_R\left(1 - \frac{\Gamma}{G}\right). \tag{1}$$

In this expression, v_R is the Rayleigh wave velocity, Γ is the fracture energy, and G is the energy release rate. The link between the previous wafer-scale measurements and the crack microstructure is thus important: the crack self-propagates within a heterogeneous medium including pressurized cracks acting as drivers for propagation, the G term, and uncracked areas that slow down the propagation, the Γ term. Note that we neglect here the influence of outer boundaries: Marder[28,29] has shown that this confers some inertia to the fracture front, hence being specially important during the acceleration phase of the front only.

We have measured the asymptotic crack velocity as a function of the split temperature (Fig. 3) for samples having received the same annealing thermal budget (450 °C–100 min). At the highest temperatures, high crack speed velocities have been reached as expected in brittle crystalline materials.[16,30–32] The data could be fit using expression (1) where G, due to pressurized cavities, is supposed to depend linearly on temperature. Indeed, the elastic stress energy associated to an individual microcrack of volume V at a pressure P is $1/2PV$ hence proportional to T if we assume that ideal gas law applies for the gas in the cavities

$$v = v_R\left(1 - \frac{A}{T}\right). \tag{2}$$

The value of the v_R parameter obtained from the fit ($v_R = 5000 \pm 200$ m/s) is close to the actual Rayleigh velocity in silicon, indicative of a minor role of dissipative instabilities such as crack branching.[33,34] This is certainly due to the weakened implanted layer of the Smart Cut™ technique that guides the crack path. The second parameter A can be

expressed as the ratio of the fracture energy Γ to the energy release rate due to pressurized cavities G_0 at ambient temperature T_0, or alternatively as $2\Gamma/Nk_B$ where N is number of gas molecules compressed in microcracks per unit surface area and k_B is the Boltzmann constant.

From the data, a ratio $\Gamma/G_0 = 0.8$ is obtained. This rather low velocity ratio is consistent with a limited crack surface coverage ($c = 60\%$, see Penot *et al.*[2] and below).

The intensity oscillations in the signal after the crack front crossing can be used to recover the deformation profile of the sample behind the fracture wave. After separation, the crack opening between two silicon arms makes an air wedge where the laser beam can experience multiple partial reflections producing interference fringes. Fringe counting allows the crack opening displacement to be measured as the transmitted intensity reaches maxima for

$$\frac{2\pi}{\lambda} nd\cos\varphi = k\pi \iff d = \frac{k\lambda}{2}, \quad k \in N, \tag{3}$$

where n is the refractive index of the air, φ is the angle of incidence of the laser beam, λ is the laser wavelength, and d is the distance between the two arms. Therefore, the interference fringe spacing observed on the laser signal after the first intensity fall corresponds to an increase of the crack air gap thickness of half the laser wavelength. During the first series of oscillations (0–20 μs), the two newly separated wafers drift apart because of the strong internal pressure release of the gas-filled microcracks. The internal energy released during the crack opening separates the silicon beams by several micrometres. However, this expansion does not carry on forever. After some time, due to gap (volume) expansion, the internal pressure drops to values below the atmospheric pressure, which exerts a restoring force on the diverging arms. The gap reaches a maximum where the external atmospheric pressure has counteracted the inertia of the two silicon arms diverging movement. This inversion point corresponds to the first large oscillation at $t = 22$ μs on laser 1 (L1) in Fig. 2. Subsequently, the motion inverts and the wafers get closer again until reaching a minimum where the internal pressure enables the two beams to pull away again. This phase corresponds to the second series of oscillations (22–50 μs on L1) where one signal oscillation corresponds now to a decrease of the air gap of $\lambda/2$. The new inversion appears at $t = 50$ μs and the two silicon arms start to diverge again. The deformation profile of the silicon arm behind the fracture wave can therefore be deduced by simply counting the number of oscillations in the laser signal after the crack crossing (Fig. 4). Note that the horizontal scale has been obtained from the time scale assuming a constant velocity motion of the crack front, which has been experimentally checked through the similarity of the profiles obtained from the four lasers.

In the example, the maximum height of the air gap is about 18 μm and is reached during the first opening of the gap. It is due to the expansion of the hydrogen gas trapped inside microcracks. The wavelength of the strip deformation profile is around 9 cm and the maximum vertical speed of displacement is around 0.5 μm/μs.

The dynamics of this motion can be modelled using beam elasticity and thermodynamics. We consider here a

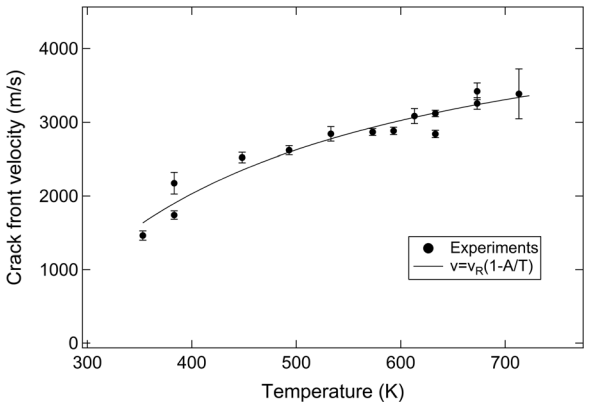

FIG. 3. Variation of the crack velocity as a function of split temperature. Solid line is a fit according to expression (1).

silicon strip of width a issued from two bonded silicon wafers of thickness h. We note $\zeta(x,t)$ the deformation of an individual wafer, i.e., half of the air gap between the two wafers during the Smart Cut™ fracture. The dynamical evolution of the air gap is given by a standard elasticity equation

$$\frac{Eh^3 a}{12(1-\sigma^2)}\frac{\partial^4\zeta}{\partial x^4} + (\rho a h)\frac{\partial^2\zeta}{\partial t^2} = P(x)a, \tag{4}$$

where E is the silicon Young's modulus, σ is the Poisson's ratio, ρ is the volumetric mass density, and P is the pressure forces resultant, i.e., the difference between the internal pressure caused by the hydrogen filled microcracks and the atmospheric pressure. The first two terms in this equation correspond to the bending rigidity restoring force and to inertial terms, respectively, while the right-hand side stands for the external forces. As seen earlier, the fracture velocity is constant along the sample so we can write the following equivalence:

$$\frac{\partial^2\zeta}{\partial t^2} = v^2\frac{\partial^2\zeta}{\partial x^2}, \tag{5}$$

where v is the fracture velocity. If we replace (5) in (4), we can deduce the following differential equation for the deformation profile:

$$\frac{\partial^4\zeta}{\partial x^4} + \frac{1}{\Lambda^2}\frac{\partial^2\zeta}{\partial x^2} = \frac{12(1-\sigma^2)P(x)}{Eh^3}, \qquad \Lambda = \frac{1}{\sqrt{12}}\frac{hc}{v}, \quad c = \sqrt{\frac{E}{\rho(1-\sigma^2)}}, \tag{6}$$

where Λ is the characteristic wavelength and c a sound wave velocity. We can first resolve Eq. (6) without the right-hand side. For $v = 1700\,\mathrm{m\ s^{-1}}$ and $c = 7700\,\mathrm{m\ s^{-1}}$, we find $\Lambda = 1$ mm, which is much smaller than the experimental wavelength of 9 cm (Fig. 4). This result shows that the fourth derivative bending term of Eq. (6) can be neglected in comparison with the inertial term. Finally, Eq. (6) can be written as

$$h\rho v^2\frac{\partial^2\zeta}{\partial x^2} = P(\zeta) - P_{atm}. \tag{7}$$

Gas expansion first accelerates crack opening, and then atmospheric pressure acts as a restoring force to bring back

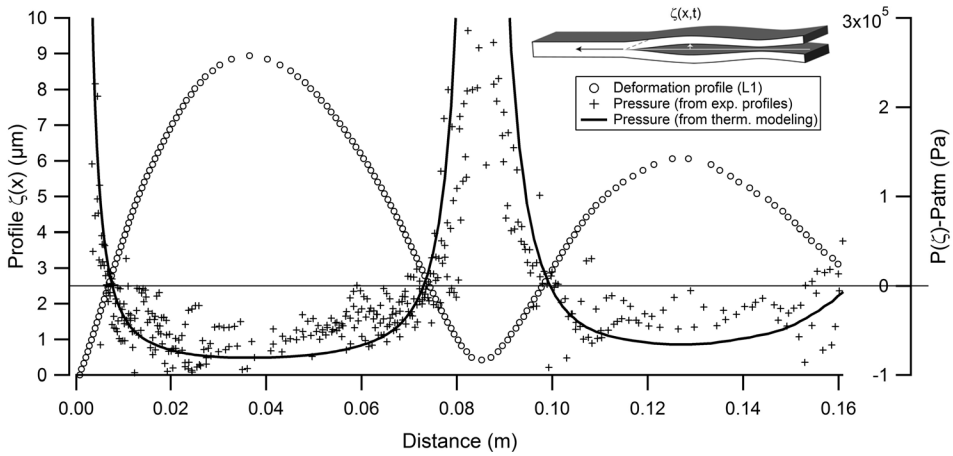

FIG. 4. Open circles (left scale): Deformation profile of the strip as obtained from L1 measurement. Crosses (right scale): pressure distribution as obtained by second derivative of the measured deformation profiles. Solid line: model of pressure evolution using adiabatic expansion.

the wafers one against the other. The system oscillates like a pneumatic piston. Experimentally, we could measure the crack opening profile using interference fringes. Hence, from (7), by differentiating twice the air gap height $\zeta(x)$, it is possible to obtain the internal pressure $P(\zeta)$ as shown in Fig. 4.

From a thermodynamics point of view, the following relation can be written for an adiabatic and reversible expansion:

$$P(\zeta)\zeta^{\gamma} = P_0\zeta_0^{\gamma}, \tag{8}$$

where $\gamma = 1.4$ is the adiabatic index. P_0 and ζ_0 can be chosen as P_{inf} and ζ_{inf}, the internal pressure and the air gap half-height at the inflection point where $P_{inf} = P_{atm}$ and $\zeta_{inf} = 2.5\,\mu$m. It is therefore possible to model the evolution of the internal pressure with the wafer separation distance. The result is shown in Fig. 4 (solid line). The curve fits well the experimental pressure data deduced from (7).

Thermodynamics further allows one to deduce the amount of gas released during the crack opening. To do so, we express the variation of internal energy between the initial situation just after the crack opening ($t = t_0$) and the first maximum of the air gap opening ($t = t_{max}$).

$$U_0 = \frac{5}{2}P_{\max}d_{\max} + P_{atm}(d_{\max} - d_0), \tag{9}$$

where d stands for the air gap opening ($d = 2\zeta$). This means that the change of internal energy corresponds to the work of pressure forces against the atmospheric pressure. d_0 corresponds to an equivalent air gap height just after the crack opening, so it can be neglected in comparison with $d_{max} = 2\zeta_{max}$ which is about 18 μm. Using ideal gas law, expression for U_0 would simply relate to the amount of gas through $U_0 = 5/2\rho_0 k_B T_0$, where ρ_0 is the number of hydrogen molecules per surface area. For $P_{max} \approx 2 \times 10^4$ Pa (see Fig. 4) and a split temperature T_0 of 383 K, we would obtain a released dose of hydrogen atoms of $\rho_s = 2\rho_0 = 3.7 \pm 0.3 \times 10^{16}$ H/cm^2 (the standard deviation results from the analysis of each laser signal). In reality, optical IR measurements of microcracks prior to fracture show that the initial pressure P_0 can reach 100 MPa so that significant deviations from ideal gas law are expected. For hydrogen, a factor of two between real and ideal gas densities at 100 MPa is expected due to molecular interactions.[35] Hence, the calculated dose should be reduced accordingly. If we compare this amount with the dose of implantation, we find that only $32 \pm 3\%$ of the hydrogen is released during the silicon layer transfer. This value is consistent with previous studies[2] where released hydrogen was measured using a calibrated mass spectrometer. For large annealing, the amount of gas released saturated to slightly more than 30% of the implanted dose. The study showed that the amount of released gas is proportional to the area covered by microcracks but because of hydrogen trapping in silicon, microcracks are able to collect only 50% of the available hydrogen from platelets below and above the microcracks plane. For a thermal split, the area covered by microcracks is about 60% of the sample surface. Therefore, the fraction of hydrogen that is released during a thermally induced split is around 30% of the implanted dose.

In summary, an original way of monitoring fracture dynamics in silicon has been proposed and applied to study the Smart Cut™ technology. Fracture speeds in the km/s range have been found, and the evolution of crack velocity with the split temperature has been studied. An asymptotic speed close to the Rayleigh velocity has been found, indicative of a minor role of dissipative instabilities. The crack opening displacements in the wake of the fracture front have also been deduced from the interference fringes in the laser signal. This allows the dynamics of this motion to be fully modelled using beam elasticity and thermodynamics. The amount of gas released during the opening was found to be around 35% of the implanted dose, which is in quantitative agreement with previous studies based on mass spectroscopy.

We would like to acknowledge support from the French authorities through the "Investissement d'Avenir" EXACT program.

[1]M. Bruel, Electron. Lett. **31**, 1201 (1995).
[2]J. D. Penot, D. Massy, F. Rieutord, F. Mazen, S. Reboh, F. Madeira, L. Capello, D. Landru, and O. Kononchuk, J. Appl. Phys. **114**, 123513 (2013).
[3]L. Capello, F. Rieutord, A. Tauzin, and F. Mazen, J. Appl. Phys. **102**, 026106 (2007).
[4]J. Grisolia, G. Ben Assayag, A. Claverie, B. Aspar, C. Lagahe, and L. Laanab, Appl. Phys. Lett. **76**, 852 (2000).
[5]S. Personnic, K. K. Bourdelle, F. Letertre, A. Tauzin, N. Cherkashin, A. Claverie, R. Fortunier, and H. Klocker, J. Appl. Phys. **103**, 023508 (2008).
[6]N. Cherkashin, S. Reboh, A. Lubk, M. J. Hytch, and A. Claverie, Appl. Phys. Express **6**, 091301 (2013).
[7]X.-Q. Feng and Y. Huang, Int. J. Solids Struct. **41**, 4299–4320 (2004).

[8]S. Reboh, F. Rieutord, L. Vignoud, F. Mazen, D. Landru, M. Zussy, and C. Deguet, Appl. Phys. Lett. **103**, 181911 (2013).
[9]F. Rieutord, B. Bataillou, and H. Moriceau, Phys. Rev. Lett. **94**, 236101 (2005).
[10]H. Moriceau, F. Rieutord, F. Fournel, Y. Le Tiec, L. Di Cioccio, C. Morales, A. M. Charvet, and C. Deguet, Adv. Nat. Sci.: Nanosci. Nanotechnol. **1**, 043004 (2010).
[11]S. Reboh, J. F. Barbot, M. F. Beaufort, and P. F. P. Fichtner, Appl. Phys. Lett. **96**, 031907 (2010).
[12]K. Ravi-Chandar, *Dynamic Fracture* (Elsevier, Oxford, 2004), pp.104–106.
[13]W. F. Riley and J. W. Dally, Exp. Mech. **9**, 27N (1969).
[14]B. Stalder, P. Beguelin, and H. H. Kausch, Int. J. Fract. **22**, R47 (1983).
[15]J. Fineberg, S. P. Gross, M. Marder, and H. L. Swinney, Phys. Rev. Lett. **67**, 457 (1991).
[16]T. Cramer, A. Wanner, and P. Gumbsch, Phys. Status Solidi A **164**, R5 (1997).
[17]D. Sherman, J. Mech. Phys. Solids **53**, 2742 (2005).
[18]A. Ball and B. W. Payne, J. Mater. Sci. **11**, 731 (1976).
[19]E. Sharon, G. Cohen, and J. Fineberg, Nature **410**, 68 (2001).
[20]I. Beery, U. Lev, and D. Sherman, J. Appl. Phys. **93**, 2429 (2003).
[21]F. Mazen, F. Rieutord, J. D. Penot, and P. Montmayeul, "System for measuring a zone of separation in a substrate," WO/2013/140065 (26 September 2013).
[22]$E = 169$GPa, $\nu = 0.062$, dilatational wave speed $v_l = 9183$ m s^{-1}, transverse wave speed $v_s = 5869$ m s-1, Rayleigh wave speed $v_R = 4490$ m s^{-1} (from Refs. 23–26).
[23]M. A. Hopcroft, J. Micro. Syst. **19**, 229 (2010).
[24]C. H. Cho, Curr. Appl. Phys. **9**, 538 (2009).
[25]O. Madelung, U. Rössler, and M. Schulz, *Group IV Elements, IV–IV and III-V Compounds. Part a - Lattice Properties* (Springer, Berlin, Heidelberg, 2001), Vol. 41A1a, pp. 1–7.
[26]T. Cramer, A. Wanner, and P. Gumbsch, Z. Metallkd. **90**, 675 (1999).
[27]L. B. Freund, *Dynamic Fracture Mechanics*, Cambridge Monographs on Mechanics and Applied Mathematics (Cambridge University Press, 1998).
[28]M. Marder, Phys. Rev. Lett. **66**, 2484 (1991).
[29]E. Bouchbinder, T. Goldman, and J. Fineberg, Rep. Prog. Phys. **77**, 046501 (2014).
[30]D. Hull and P. Beardmore, Int. J. Fract. Mech. **2**, 468 (1966).
[31]J. A. Hauch, D. Holland, M. P. Marder, and H. L. Swinney, Phys. Rev. Lett. **82**, 3823 (1999).
[32]T. Cramer, A. Wanner, and P. Gumbsch, Phys. Rev. Lett. **85**, 788 (2000).
[33]K. Ravi-Chandar and W. G. Knauss, Int. J. Fract. **26**, 141 (1984).
[34]E. Sharon, S. P. Gross, and J. Fineberg, Phys. Rev. Lett. **74**, 5096 (1995).
[35]E. W. Lemmon, M. O. McLinden, and D. G. Friend, "Thermophysical properties of fluid systems," in *NIST Chemistry WebBook, NIST Standard Reference Database Number 69*, edited by P. J. Linstrom and W. G. Mallard (National Institute of Standards and Technology, Gaithersburg, 2015).